# Turbulent transition of a gaseous mixing zone induced by the Richtmyer-Meshkov instability

Yannick Bury,[1,*] Pierre Graumer,[1] Stéphane Jamme,[1] and Jérôme Griffond[2]
[1]*ISAE-SUPAERO, Université de Toulouse, France*
[2]*CEA, DAM, DIF, Arpajon F-91297, France*

(Received 4 September 2019; accepted 21 January 2020; published 27 February 2020)

This paper provides insights into the process driving the fast transition of an impulsively accelerated, then decelerated interface between gases of different densities, such as the one produced by the Richtmyer-Meshkov instability, when the timescale of this transitional process is of the same order as the characteristic timescales representative of the resulting turbulence. In this context, a new experimental approach is exposed. For the first time, it allows to design well-defined initial gaseous interfaces in a multiparametric and controlled way, giving access to a precise statistical analysis of the flow. An overview of the main results obtained by means of strioscopic, particle image velocimetry and tomoscopic measurements is provided. They unravel the fast transition of the mixing zone to a turbulent state, as the imprint of the initial condition is lost and the dynamical spectral content covers a wide range of scales, compatible with the achievement of a self-similar trend on very short timescales.

DOI: 10.1103/PhysRevFluids.5.024101

## I. INTRODUCTION

The transitional process towards a turbulent state of a Richtmyer-Meshkov (RM) instability-induced turbulent mixing zone is experimentally addressed in this paper. This instability occurs when an interface between fluids of different densities is impulsively accelerated by an incident shock wave (ISW), like in inertial confinement fusion experiments where it promotes the development of a turbulent mixture preventing the achievement of self-ignition. Many experimental studies have been devoted to the analysis of the linear [1–3] and then nonlinear development stages of such flows [4–6]. Nevertheless, later development phases, including subsequent interactions with a reflected shock wave (RSW, reshocked phase), are much less documented [7,8] and still raise fundamental questioning about the dependence of the mixing zone postreshock evolution on its more or less turbulent prereshock state. More generally, how, and up to which extent, do the ISW/initial interface interaction-induced disturbances evolve in the resulting heterogeneous density medium until the sudden deceleration of the main flow, if this occurs soon after the impulsive acceleration, when the flow is still experiencing its transient effects? Is the self-similar character, typical of developed turbulence, attainable? The more or less developed turbulent state of the flow remains difficult to evaluate in this particular context where perturbations evolve in highly transient environments, where the timescale of the transitional process is of the same order as the characteristic timescales representative of the resulting turbulence. One of the indicators of the evolution of the flow towards a fully turbulent state is the forgetting of initial conditions [9], which must result in a redistribution of energy over a wide range of spatial and temporal flow scales. It

*yannick.bury@isae.fr

 

is therefore necessary to precisely characterize these initial conditions to evaluate the evolution of their signature within the flow and thus infer the occurrence, or not, of the turbulent regime. To date, the experimental identification of the mechanisms underlying these transitional regimes is still challenging.

The operational lock for an accurate control of the initial and boundary conditions and for the implementation of relevant measurement methods allowing the comprehensive study of these flows largely explains this challenge. It is indeed essential to ensure a limited diffusion of the two species initially located on both sides of the interface, in order to guarantee a strong enough density contrast. By providing a well-known and customizable spatial disturbance pattern, it should also pave the way for a parametric study of the turbulent transition of the mixing zone.

To date, two main strategies have been developed to tackle this challenge. The first historically deployed strategy relies on an initial, solid or soft physical separation between the two gaseous species [2,7,10–15]. A more recent experimental strategy aims at getting rid of any physical separation between the two gases by generating diffuse shear layers or curtains [8,16–19].

If these various strategies have partially, or even mostly for a few of them, met the objective of quantifying the late development of the mixing zone, they still rise questions about the necessary determination and control of both initial and boundary conditions. The latter are indeed *sine qua non* conditions for a comprehensive investigation of the memory effects during the turbulent transition process inside the mixing zone.

The present study addresses these issues. A new experimental protocol is designed to promote a rapid transition to turbulence of an impulsively accelerated (shock) then decelerated (reshock) two-species mixing zone. This protocol is associated with an experimental setup, based on a multiple rotating shutter system, hereafter denoted MR2S. This setup relies on a membraneless system designed to strongly limit the initial molecular diffusion between the two gases. Moreover it guarantees the repeatability of the experiment and allows for a comprehensive characterization and control of the initial conditions, giving access to a precise statistical, ensemble-average-based analysis of the flow.

## II. METHODS

The experimental setup, sketched in Fig. 1, consists in a 5-m-long, 130-mm-square cross section vertical shock tube. A shock wave (Mach number $M = 1.2$) travels upwards and crosses an air/helium interface, which sets the Atwood number to 0.76. The MR2S separates air from helium located inside the $L = 300$ mm-long test section.

The generation of a weakly diffused, periodic initial gaseous interface is ensured by multiple rotating shutters in the form of series of equally distributed parallel blades of $130 \times \lambda$ mm$^2$ rectangular shape, where $\lambda$ is the width of the blades. Here $\lambda = 10$ mm. Each blade can rotate around a central pivot corresponding to its axis of symmetry, according to an adaptable opening law $\omega(t)$. The pivot is located at $X = 0$ mm, which defines the mean position of the initial interface (Fig. 1). The rotation of the blades is achieved by transforming the controlled linear movement of two magnetic cylinders, positioned outside of the test section, into a rotational movement of the blades *via* two miniaturized crankshaft/connecting rod systems. Each of the two "magnetic cylinder/crankshaft/rod" system drives the even- or odd-numbered interconnected blades, respectively. The total opening time of the MR2S can be adjusted from 5 ms $\pm 0.1\%$ to 100 ms $\pm 0.1\%$ by fitting the linear velocity law of the two magnetic cylinders. This allows to generate varieties of initial conditions. The repeatability of the flow structure produced by the MR2S from one shot to another was verified through a series of 50 independent tests. It relied on the analysis of the initial gaseous interface shape obtained from tomoscopic and PIV measurements, before the passage of the incident shock wave (ISW, see, e.g., Fig. 2).

The generation of the SW is triggered by a dedicated synchronization system so that the traveling ISW interacts with the initial gaseous interface at a precisely controlled instant $\tau$ after the opening of the blades. Here $\tau$ was fixed equal to 4 ms as a "safety" time lap, to secure the blades in case

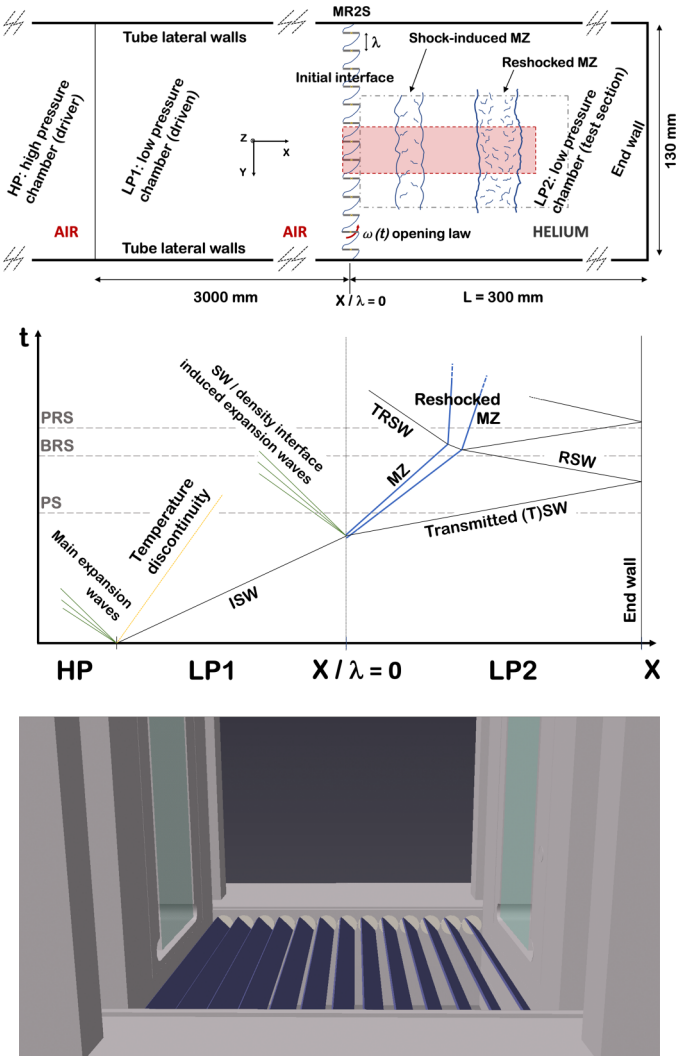


FIG. 1. Top: Schematic of the experimental test bench and measurement zones (tilted horizontally for convenience). Rectangles in gray and red dashed lines depict strioscopic and PIV/tomoscopic fields of view, respectively. The mixing zone is illustrated at different characteristic instants (blades are opened); center: wave diagram of the experiment; bottom: detailed view of the blades partly opened (here at 45°).

the MR2S device would experience any hazardous opening latency due to triggering issues. The synchronization system also triggers the different diagnostic methods for the characterization of the mixing process at the moments of interest.

Time-resolved Schlieren, two-component PIV, and laser tomoscopic measurements are conducted in the central $(X, Y)$ plane of the test section ($Z = 0$ mm), giving access to the streamwise evolution of the mixing zone, from the inception of the initial gaseous interface by the MR2S at $X/\lambda = 0$ to the reshocked phase, up to $X/\lambda \approx 11$. The spanwise dimension of the measurement zone is fixed to approximately 2.5 λ, centered around $Y/\lambda = 0$. For PIV measurements the flow seeding, composed of 0.8 $\mu$m (based on the mean Sauter diameter $D_{32}$) oil-based spherical particles, is ensured in the entire test section and on both sides of the initial interface. In the present investigation, the optimal time interval between the two laser pulses used for the determination of a velocity vector

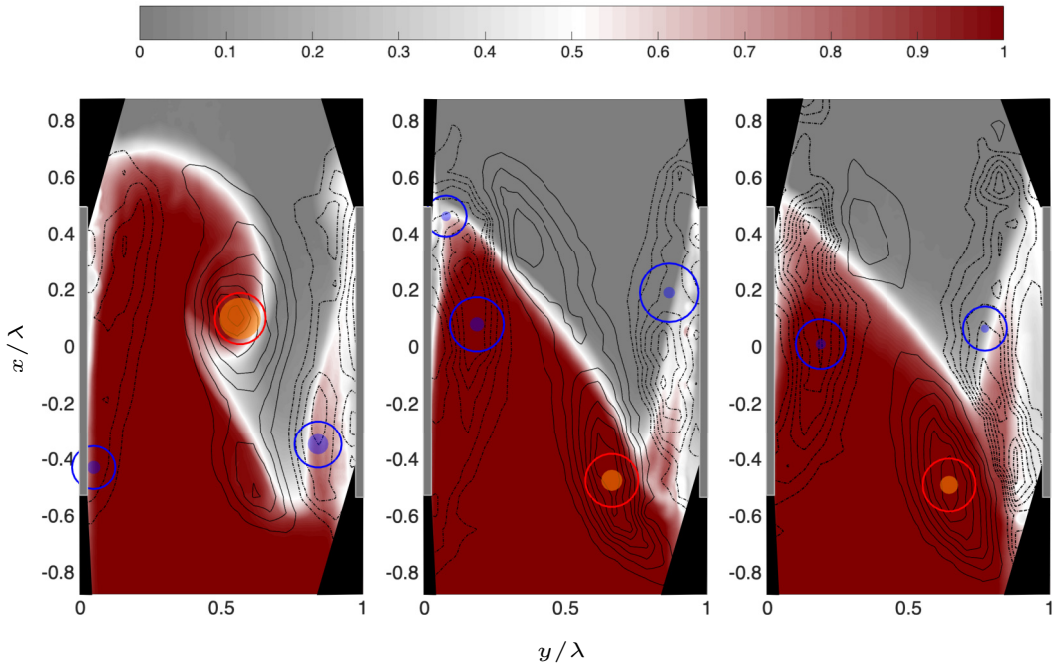


FIG. 2. Isocontours of instantaneous air mass fraction superimposed with out-of-plane vorticity isolines (dashed: negative, solid: positive) measured at $\tau = 4$ ms after the complete opening of the blades (blade rotation is counterclockwise), for an opening time of 10 ms (left), 21 ms (center), and 30 ms (right). Circles and disks symbolise vortex core diameter and strength (based on $\lambda_2$ criterion [21], with a $\lambda_2$ threshold arbitrarily fixed to $-1000$, as this value does not impact significantly the computed vortex parameters), respectively (blue/red for negative/positive vorticity). Vortex core diameters are proportional to circle diameters and scale with figure size. Solid disk diameters are proportional to vortex strength, with a scaling arbitrarily fixed such that 0.004 $m^2/s \Leftrightarrow 0.2y/\lambda$. Black zones are saturated regions associated with laser sheet reflections.

map is equal to 5 $\mu$s. For the tomoscopic measurements, only one species—in the present case the air—is seeded. Moreover, the seeding density must be slightly increased in comparison to PIV, to guarantee homogeneous gray level fields of the seeded species, relevant to derive density fields [20].

## III. RESULTS

We focus on the analysis of the mixing zone, from the generation of the initial interface by the MR2S to the postreshocked instants. Various initial conditions, imposed by different opening times of the blades 10 ms, 21 ms, and 30 ms, are first described. The analysis of the evolution of the shocked/reshocked mixing zone is then conducted for an opening time of 21 ms. This opening time was chosen as a compromise to limit the mechanical efforts on the MR2S device, which increase as the opening time is reduced, while ensuring a weakly diffused initial interface favorable to the RM instability-induced baroclinic production.

### A. Initial conditions

Figure 2 shows the air mass fraction field superimposed with the vorticity field obtained from tomoscopic and PIV measurements, 4 ms after the complete opening of the blades, before shock arrival, for three different opening velocities of the MR2S. These results highlight a weakly diffused interface. Moreover, series of prevalidation tests were conducted to estimate the impact of the sole diffusion process on the thickening of the initial interface as a function of time in regard to

the complete mixing process following the shock-reshock phases. They revealed the negligible contribution of the diffusion on the overall mixing mechanisms. Figure 2 also shows that, while the MR2S device does not induce significant interblade velocity fields during and after the blades opening (maximum of few tens of cm/s, far below the fluctuation levels induced after the passage of the ISW, of the order of a few tens of m/s; see Fig. 3), the obtained patterns provide, however, complex interface deformations, from monotonous for the longest opening time to nonmonotonous for the shortest ones. This is favorable to ensure a significant misalignment between local pressure and density gradients when the SW travels through the species interface. These measurements also reveal the occurrence of a starting vortex at the tip of the blades, whose intensity depends on the local Reynolds number. This Reynolds number is related to the velocity at the tip of the blades, but even more to the physical properties of the gaseous medium in which each of the tips is plunging into (He vs air). Indeed, the vortex is more intense when the blade tip has plunged inside air (higher Reynolds number, orange disks in Fig. 2). Moreover, the variation of the opening velocity law noticeably impacts the pattern of the initial gaseous interface. Interestingly enough, the starting vortex experiences a separation from the blade when the opening velocity is high enough. Here this happens for the fastest opening velocity [Fig. 2 (left)]. This vortex locally deforms the initial interface as it moves upwards, still increasing the complexity of the pattern. The position of the vortex at the instant of the ISW/interface interaction can be varied by changing the time lag $\tau$ between the complete opening of the blades and the crossing of the ISW. This is of prime interest as it offers an additional flow control parameter for the shaping of the initial interface, in addition to the more intuitive wavelength $\lambda$ and blade velocity opening law $\omega(t)$.

### B. Postshock phase

Once the initial interface has been shaped as preset by the MR2S with an opening time of 21 ms, it first experiences a sudden acceleration at the moment the ISW crosses the interface ($t = 0\ \mu$s), promoting the inception of a traveling mixing zone. This shock wave then reflects at the top end-wall of the tube and travels back towards the developing mixing zone. A few instants later (at $t \approx 450\ \mu$s), the RSW impacts the developing mixing zone which then undergoes a sudden deceleration (Fig. 1). The following analysis focuses on three key instants of the evolution of the subsequent mixing process: just after the crossing of the ISW ($t \approx 130\ \mu$s, noted PS), just before the interaction of the mixing zone with the RSW ($t \approx 420\ \mu$s, noted BRS), and immediately following this interaction ($t \approx 550\ \mu$s, noted PRS).

Figure 3 depicts, from left to right and for the three previously mentioned key instants, the following: instantaneous Schlieren images of the mixing zone; 2D isocontours of mean air mass fraction (based on ensemble average of 65 experiments) superimposed with out-of-plane mean vorticity isolines; 2D isocontours of turbulent kinetic energy (TKE) $\mathcal{K} = (\overline{u_x'^2} + \overline{u_y'^2})/2$ (with $u_x'$ and $u_y'$ the fluctuating components of the velocity along $x$ and $y$ directions respectively); and power spectral density (PSD) maps of TKE computed along the $y$ direction for each $x$ position.

For the early stage of its development [PS, Fig. 3(a)], the mixing zone still bears the imprint of the periodic pattern imposed by the initial condition. This translates on Schlieren and tomoscopy images into periodically distributed mushroom-like spots (see, e.g., $Y_{\text{air}} = 0.05$ air mass fraction isoline) and into comma-shaped pockets of higher TKE levels. The large-scale air-helium mixing is characterized by the penetration of air spikes into helium, highlighted by, e.g., the shape of the $Y_{\text{air}} = 0.5$ air mass fraction isoline. Well-defined connex vorticity pockets of opposite sign are distributed on both sides of the spikes, inside the helium bubbles. Two counterrotating vortices are identified in the core of these vorticity pockets. These vortices affect the mixing process by deforming the shape of both spikes and bubbles. The most intense structure (depicted in blue), issued from the baroclinic deposition of vorticity following the interaction of the ISW with the initial density interface, transfers helium inside the bubbles in a counterclockwise motion. The second structure (orange disk), resulting from the diffraction of the ISW at the upper tip of the blades, deforms the head of the spike into a hook shape. This results in the loss of symmetry of

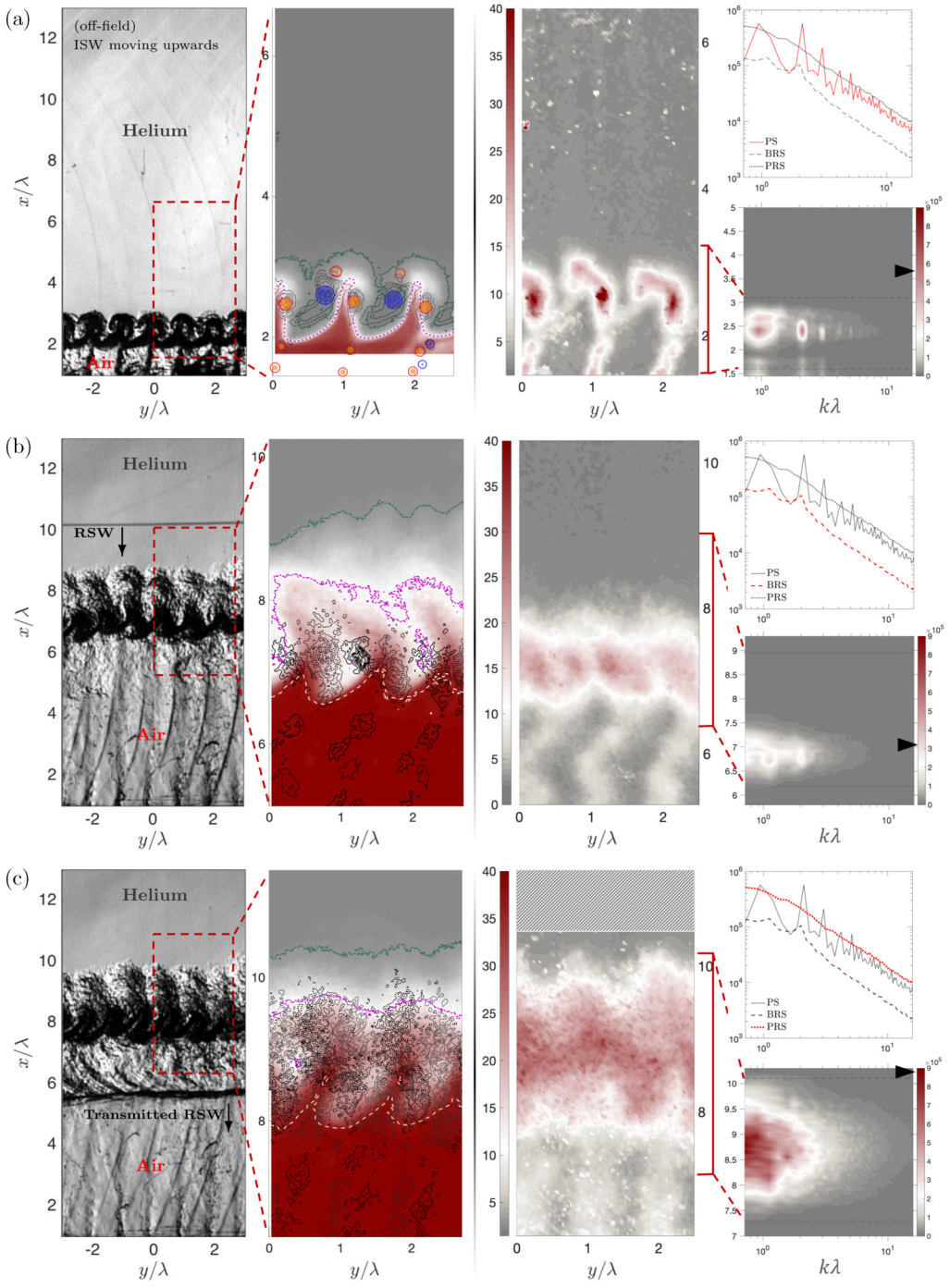


FIG. 3. From left to right: snapshots of Schlieren images of the mixing zone; 2D isocontours of air mass fraction (white, purple, and green dashed lines correspond to 0.95, 0.5, and 0.05 isolines, respectively. Circles and disks as in Fig. 2, with 0.6 $m^2/s \Leftrightarrow 0.3y/\lambda$) superimposed with out-of-plane vorticity isolines (dashed: negative, solid: positive); 2D isocontours of turbulent kinetic energy TKE ($m^2\,s^{-2}$); and (lower graph) TKE PSD maps (black cursor indicates the maximum energy level) with (upper graph) 1D extracted profiles in the central zone. (a) PS, (b) BRS, and (c) PRS instants.

both bubbles and spikes. The content of the PSD map correlates with the previous observations. Two principal peaks are clearly distinguishable in the central area of the mixing zone, at $x/\lambda \approx 2.4$, for wave numbers $k\lambda = 1$ and $k\lambda = 2$. The first peak corresponds to the periodic scheme imposed by the interblade geometry of the MR2S. The second peak reflects the occurrence of the two previously evoked counterrotating vortices. Furthermore, harmonics of the two main wave numbers fuel the high wave-number range of the PSD map, as shown in particular on the 1D spectrum extracted at $x/\lambda = 2.4$, in the center of the mixing zone. Finally, the smaller vortices identified on the bottom part of the composite tomoscopic image, for $x/\lambda < 1.9$ (also visible as vertical strips on the Schlieren images), result from the shedding process at the blade trailing edges.

### C. Prereshock phase

Just before the interaction of the RSW with the mixing zone [BRS, Fig. 3(b)], the large-scale periodic scheme can still be identified, indicating the still-partial persistence of the initial condition in the flow. However, the Schlieren image of the mixing zone depicts a more granular aspect, most probably associated with the development of lower-scale structures. This also translates into more gradual variations of the air mass fraction on 2D fields, as well as the fragmentation of the vorticity pockets, revealing the enhancement of the mixing. The 2D map of TKE emphasizes the homogenization of the velocity fluctuations in the lower part of the mixing zone, in regions of higher density contrasts associated with higher shock-induced baroclinic production. The analysis of the TKE PSD map reinforces this hypothesis. Indeed, the two peaks associated with the initial condition are strongly damped. The PSD map also exhibits the spreading of the wave-number range, in conjunction with an attenuation of the global energy level (see black cursor levels on the PSD scales for PS and BRS instants). These trends are also emphasized on the 1D extracted spectra when compared from PS to BRS instants.

### D. Postreshock phase

Immediately after the interaction of the RSW with the mixing zone [PRS, Fig. 3(c)], the mixing process strongly increases. In particular, the mixing zone features more uniformly distributed air mass fraction mapping, especially in its lower half. Moreover, the recompression imposed by the reshock results in more intense air mass fraction gradients in the upper part of the mixing zone, as evidenced by the closest proximity between $Y = 0.05$ and $Y = 0.5$ air mass fraction isolines (compared with the distance between $Y = 0.5$ and $Y = 0.95$ isolines). Vorticity and TKE 2D fields are also strongly impacted by the reshock phenomenon. This is revealed by the noticeable spreading and fragmentation of the vorticity isolines and by the increased extent of the velocity fluctuations inside the mixing region, as a result of the new baroclinic deposition of vorticity when the RSW travels across the developing mixing zone. At last, the wave-number content of the kinetic energy PSD map and 1D spectrum do not depict any energy peak anymore, whereas the global energy level has strongly increased on the whole range of wave numbers (see black cursor level on the PSD scales for PRS compared to BRS).

### E. Turbulent transition criteria of the mixing zone

In addition to the above characterization of the mixing zone, the analysis of its turbulent transition was also conducted based on transition criteria as defined in the literature (see Dimotakis [22] and Mohaghar [18]). These transition criteria should reflect the existence of an inertial range in the turbulence spectrum, which must translate into a noticeable separation between the energetic and dissipative scales. The upper limit of the inertial range is commonly defined as the Liepmann-Taylor scale $\lambda_L \approx 2.17\lambda_T$ [22], where $\lambda_T$ stands for the Taylor microscale (here $\lambda_T$ is the mean of the streamwise and spanwise Taylor microscales, computed from the curvature of the velocity autocorrelation function [19] obtained from the PIV measurements). The upper bound of the dissipative range, also denoted inner-viscous length scale, is defined as $\lambda_\nu = 50\lambda_K \approx 50\,\delta\,\mathrm{Re}^{-3/4}$,

TABLE I. Overall comparison of the considered transition criteria at different instants PS, BRS, and PRS of the development of the mixing zone. For a given definition of the Reynolds number, as described in the core of the text, the corresponding scale $\lambda_\nu$ and associated scale ratio $\lambda_L/\lambda_\nu$ are provided in the adjacent columns. Values in the second headings row correspond to the referenced thresholds for the different turbulent transition criteria [22,23].

| Instants | $\lambda_T$ (mm) | $\mathrm{Re}_h$ $\approx 10^4$ | $\lambda_\nu$ (mm) | $\frac{\lambda_L}{\lambda_\nu}$ 1–10 | $\mathrm{Re}_\mathcal{K}$ $\approx 10^4$ | $\lambda_\nu$ (mm) | $\frac{\lambda_L}{\lambda_\nu}$ 1–10 | $\mathrm{Re}_{\lambda_T}$ 100–140 | $\lambda_\nu$ (mm) | $\frac{\lambda_L}{\lambda_\nu}$ 1–10 |
|---|---|---|---|---|---|---|---|---|---|---|
| PS | 1.38 | 24000 | 0.31 | 9.74 | 7256.8 | 0.75 | 3.97 | 844.7 | 0.44 | 6.80 |
| BRS | 1.73 | 26100 | 0.51 | 7.37 | 14577.4 | 0.79 | 4.76 | 1205.9 | 0.42 | 8.88 |
| PRS | 1.69 | 54564 | 0.33 | 11.1 | 26771 | 0.57 | 6.48 | 1911.4 | 0.29 | 12.54 |

where $\lambda_K$ is the Kolmogorov scale, $\delta$ a macroscale representative of the mixing zone and Re stands for a Reynolds number. This Reynolds number can be defined as $\mathrm{Re}_h = h\dot{h}/\nu_{\mathrm{mix}}$, with $\dot{h}$ the growth rate of the MZ width $h$, here chosen as the macroscale $\delta$ representative of the MZ, and $\nu_{\mathrm{mix}} = (\mu_1 + \mu_2)/(\rho_1 + \rho_2)$ the mean kinematic viscosity based on the dynamic viscosities and densities of species 1 and 2. The turbulent transition is then considered to be effective when $\mathrm{Re}_h > 10^4$. Mohaghar *et al.* [18] also suggest using the turbulent kinetic energy Reynolds number $\mathrm{Re}_\mathcal{K} = \sqrt{\mathcal{K}}\,h/\nu_{\mathrm{mix}}$ with a similar threshold for the turbulent transition. One can also consider the Taylor Reynolds number $\mathrm{Re}_{\lambda_T}$ [22], defined as $\mathrm{Re}_{\lambda_T} = \sqrt{\mathcal{K}}\,\lambda_T/\nu_{\mathrm{mix}}$. In this case, the turbulent transition is expected to be effective above $\mathrm{Re}_{\lambda_T} \approx 100$–$140$. Finally, the necessary separation of energetic and dissipative scales is also assessed by $\lambda_L/\lambda_\nu > 1$ [22]. A more restrictive scale separation corresponding to fully developed turbulence is even proposed by Lombardini *et al.* [23] in the form $\lambda_L/\lambda_\nu > 10$.

All these parameters are summarized in Table I. It is worth noting that, whatever the considered transition criterion, the necessary condition for an effective turbulent transition of the flow is always satisfied, except for early time PS if considering the $\mathrm{Re}_\mathcal{K}$ criterion. Interestingly enough, the ratio $\lambda_L/\lambda_\nu$ characterizing the extent of the wave-number range separating energetic and dissipative scales progressively increases as the flow first evolves after the incident shock wave passage, and then experiences the reshock phenomenon. It is even above the threshold defined by Lombardini *et al.* [23], for two of the three investigated Reynolds numbers at late PRS instant. This is in line with the spreading of the wave-number range and the increase of the mixing process inside the mixing zone, previously revealed by the PSD maps. The above analysis tends to indicate that the turbulent transition is reached at quite early stages of the mixing when the initial interface is conveniently shaped by the MR2S device. However, the above-analyzed quantitative criteria should be considered as necessary, but not sufficient, to guarantee a fully developed turbulent state [22].

## IV. CONCLUSION

In summary, this paper has demonstrated that the transition towards a turbulent state of a RM instability-induced mixing zone is attainable on a very short timescale, comparable to the characteristic timescales of the so-produced turbulence. This was made possible thanks to a new experimental approach able to impose varieties of well-characterized, strictly repeatable initial and periodic conditions. By adjusting the control parameters of the device, the misalignment between density and pressure gradients can be tuned such as to boost the RM instability-induced baroclinic production. This study relied on the combined analysis of ensemble-averaged flow fields of air mass fraction, vorticity, and turbulent kinetic energy at some key instants of the mixing development. Interestingly enough, the results reveal both the forgetting of the initial conditions and the broadband feeding of the spectral content of the velocity fluctuations, in line with a self-similar trend, representative of a turbulent flow.

**ACKNOWLEDGMENTS**

This work is supported by CEA under Grant No. CAJ-15-29 monitored by Dr. Denis Souffland. The authors gratefully acknowledge the ISAE technical staff for its valuable support in the design and operation of the experiment.

[1] R. D. Richtmyer, Taylor instability in shock acceleration of compressible fluids, Commun. Pure Appl. Math. **13**, 297 (1960).

[2] E. Meshkov, Instability of the interface of two gases accelerated by a shock wave, Fluid Dyn. **4**, 101 (1960).

[3] M. Brouillette and B. Sturtevant, Experiments on the Richtmyer-Meshkov instability: Small-scale perturbations on a plane interface, J. Fluid Mech. **263**, 271 (1994).

[4] O. Sadot, L. Erez, U. Alon, D. Oron, L. A. Levin, G. Erez, G. Ben-Dor, and D. Shvarts, Study of Nonlinear Evolution of Single-Mode and Two-Bubble Interaction Under Richtmyer-Meshkov Instability, Phys. Rev. Lett. **80**, 1654 (1998).

[5] B. Collins and J. Jacobs, PLiF flow visualization and measurements of the Richtmyer-Meshkov instability of an air/SF6 interface, J. Fluid Mech. **464**, 113 (2002).

[6] R. V. Morgan, R. Aure, J. D. Stockero, J. A. Greenough, W. Cabot, O. A. Likhachev, and J. W. Jacobs, On the late-time growth of the two-dimensional Richtmyer-Meshkov instability in shock tube experiments, J. Fluid Mech. **712**, 354 (2012).

[7] E. Leinov, G. Malamud, Y. Elbaz, L. A. Levin, G. Ben-Dor, D. Shvarts, and O. Sadot, Experimental and numerical investigation of the Richtmyer-Meshkov instability under re-shock conditions, J. Fluid Mech. **626**, 449 (2009).

[8] J. W. Jacobs, V. V. Krivets, V. Tsiklashvili, and O. A. Likhachev, Experiments on the Richtmyer-Meshkov instability with an imposed, random initial perturbation, Shock Waves **23**, 407 (2013).

[9] J. P. Eckmann, Roads to turbulence in dissipative dynamical systems, Rev. Mod. Phys. **53**, 643 (1981).

[10] L. Houas and I. Chemouni, Experimental investigation of Richtmyer-Meshkov instability in shock tube, Phys. Fluids **8**, 614 (1996).

[11] G. Jourdan, L. Houas, J.-F. Haas, and G. Ben-Dor, Thickness and volume measurements of a Richtmyer-Meshkov instability-induced mixing zone in a square shock tube, J. Fluid Mech. **349**, 67 (1997).

[12] C. Mariani, M. Vandenboomgaerde, G. Jourdan, D. Souffland, and L. Houas, Investigation of the Richtmyer-Meshkov Instability with Stereolithographed Interfaces, Phys. Rev. Lett. **100**, 254503 (2008).

[13] D. Ranjan, M. Anderson, J. Oakley, and R. Bonazza, Experimental Investigation of a Strongly Shocked Gas Bubble, Phys. Rev. Lett. **94**, 184507 (2005).

[14] L. Liu, Y. Liang, J. Ding, N. Liu, and X. Luo, An elaborate experiment on the single-mode Richtmyer-Meshkov instability, J. Fluid Mech. **853**, R2 (2018).

[15] R. Bonazza and B. Sturtevant, X-ray measurements of growth rates at a gas interface accelerated by shock waves, Phys. Fluids **8**, 2496 (1996).

[16] K. P. Prestridge, P. M. Rightley, P. Vorobieff, R. F. Benjamin, and N. A. Kurnit, Simultaneous density-field visualization and PIV of a shock-accelerated gas curtain, Exp. Fluids **29**, 339 (2000).

[17] C. Weber, N. Haehn, J. Oakley, D. Rothamer, and R. Bonazza, Turbulent mixing measurements in the Richtmyer-Meshkov instability, Phys. Fluids **24**, 074105 (2012).

[18] M. Mohaghar, J. Carter, B. Musci, D. Reylly, J. McFarland, and D. Ranjan, Evaluation of turbulent mixing transition in shock-driven variable-density flow, J. Fluid Mech. **831**, 779 (2017).

[19] D. T. Reese, A. M. Ames, C. D. Noble, J. G. Oakley, D. A. Rothamer, and R. Bonazza, Simultaneous direct measurements of concentration and velocity in the Richtmyer-Meshkov instability, J. Fluid Mech. **849**, 541 (2018).

[20] J. C. Sautet and D. Stepowski, Dynamic behavior of variable density, turbulent jets in their near development fields, Phys. Fluids **7**, 2796 (1995).

[21] Y. Bury, T. Jardin, and A. Klöckner, Experimental investigation of the vortical activity in the close wake of a simplified military transport aircraft, Exp. Fluids **54**, 1524 (2013).
[22] P. E. Dimotakis, The mixing transition in turbulent flows, J. Fluid Mech. **409**, 69 (2000).
[23] M. Lombardini, D. I. Pullin, and D. I. Meiron, Transition to turbulence in shock-driven mixing: A Mach number study, J. Fluid Mech. **690**, 203 (2012).